Subdiffuse scattering and absorption model for single fiber reflectance spectroscopy

ANOUK L. POST,[1,2,*] **DIRK J. FABER,**[1] **HENRICUS J. C. M. STERENBORG,**[1,2] **AND TON G. VAN LEEUWEN**[1]

[1]*Amsterdam UMC, University of Amsterdam, Department of Biomedical Engineering and Physics, Cancer Center Amsterdam, Amsterdam Cardiovascular Sciences, Meibergdreef 9, 1105 AZ, Amsterdam, The Netherlands*
[2]*The Netherlands Cancer Institute, Department of Surgery, Plesmanlaan 121, 1066 CX, Amsterdam, The Netherlands*
[*]*a.l.post@amsterdamumc.nl*

Abstract: Single fiber reflectance (SFR) spectroscopy is a technique that is sensitive to small-scale changes in tissue. An additional benefit is that SFR measurements can be performed through endoscopes or biopsy needles. In SFR spectroscopy, a single fiber emits and collects light. Tissue optical properties can be extracted from SFR spectra and related to the disease state of tissue. However, the model currently used to extract optical properties was derived for tissues with modified Henyey-Greenstein phase functions only and is inadequate for other tissue phase functions. Here, we will present a model for SFR spectroscopy that provides accurate results for a large range of tissue phase functions, reduced scattering coefficients, and absorption coefficients. Our model predicts the reflectance with a median error of 5.6% compared to 19.3% for the currently used model. For two simulated tissue spectra, our model fit provides accurate results.

1. Introduction

Reflectance spectroscopy techniques can provide rapid information related to the structural and biochemical composition of tissue. Single Fiber Reflectance (SFR) spectroscopy is a technique where light is emitted and collected through a single fiber, which is connected to a broadband light source and a spectrograph using a bifurcated fiber or a beam splitter. SFR measures the steady-state reflectance versus wavelength. Due to its small footprint, SFR measurements can be performed through endoscopes or biopsy needles [1–3]. SFR spectroscopy has been studied for medical diagnostics mainly in the field of oncology [2–8], but also in e.g. saturation monitoring [9] and orthopedics [1,10].

SFR spectroscopy is especially suitable to detect small-scale changes in tissue, due to its relatively small sampling volume, $\sim(100\,\mu m)^3$, and sensitivity to the tissue phase function. Since light is emitted and collected through the same fiber, photon path lengths are biased towards short pathlengths and diffusion theory alone cannot describe the measured reflectance. SFR spectroscopy is a subdiffuse technique and, therefore, measurements are sensitive to the tissue phase function [11–13], which is related to the nanoscale architecture of tissue. When light propagation is described as a random walk, the phase function (p[θ]) describes the probability of a photon scattering at an angle θ relative to the photon's previous trajectory for each scattering event.

With an appropriate model, optical properties can be extracted from SFR spectra, which can be related to the disease state of tissue. Until now, only a single model was available for SFR spectroscopy to relate the measured reflectance to scattering and absorption properties of tissue, which was derived by Kanick et al. [14,15]. The model of Kanick et al. was derived using Monte Carlo (MC) simulations with modified Henyey Greenstein (MHG) phase functions. Unfortunately,

even though the MHG phase function describes the phase function of skin tissue [16], for many other tissues other phase functions have been measured, e.g. the two-term Henyey-Greenstein (TTHG) for liver [17,18], uterus [17], brain [19], breast [20] and muscle [21] and the Reynolds McCormick phase function (RMC, also known as Gegenbauer) for blood [22,23]. In practice, the phase function of a specific tissue under investigation is generally not known. Therefore, a model that is valid for the wide range of tissue phase functions is essential.

Recently, we took the first steps towards the development of a new model for the SFR reflectance that provides accurate results for the wide range of tissue phase functions that can be encountered. We developed a new parameter (p_{sb}) to capture the phase function influence on the measured reflectance and we developed a model for the reflectance as a function of tissue scattering properties in the absence of absorption [24]. However, due to the presence of absorbers in tissue such as blood, fat, and water, it is essential that absorption is included in the model to enable accurate extraction of optical properties from tissue measurements.

In this paper, we will develop a comprehensive model for the SFR reflectance as a function of both scattering and absorption properties of tissue. Furthermore, we will validate our model based on MC simulations for the wide range of reduced scattering coefficients, absorption coefficients, and phase functions that can be encountered in tissue. We will demonstrate that our comprehensive model for SFR spectroscopy predicts the measured reflectance substantially better than the model from Kanick et al. [14,15]. Finally, we will demonstrate the use of our model to determine optical properties from SFR measurements by simulating spectra of two tissue types.

2. Methods

2.1. SFR model

Diffusion theory can accurately describe the reflectance when photon path lengths are larger than several transport mean free paths, where the transport mean free path is the inverse of the reduced scattering coefficient: $1/\mu_s'$ and the reduced scattering coefficient equals $\mu_s'=\mu_s(1-g_1)$, where μ_s is the scattering coefficient and g_1 is the scattering anisotropy (the first Legendre moment of the phase function). In SFR spectroscopy, photon path lengths are generally less than one transport mean free path since light is emitted and collected through the same fiber. In this so-called subdiffuse regime, the measured reflectance is the sum of photons undergoing a large number of scattering events (diffuse photons) and photons that undergo a few scattering events (semiballistic photons). Therefore, we model the reflectance as the sum of a semiballistic reflectance ($R_{SFR,sb}$) and a diffuse reflectance ($R_{SFR,dif}$):

$$R_{SFR} = R_{SFR,sb} + R_{SFR,dif} = (1 + X) \cdot R_{SFR,dif} \tag{1}$$

where X is the ratio between the semiballistic and diffuse reflectance:

$$X = \frac{R_{SFR,sb}}{R_{SFR,dif}} \tag{2}$$

Semiballistic photons are defined here as detected photons that underwent a single backscattering event in combination with an arbitrary number of forward scattering events [25].

Diffuse photons undergo many scattering events before they are detected and, therefore, their direction is randomized. Thus diffuse reflectance does not depend on the details of the tissue phase function, but only on the scattering anisotropy g_1. Semiballistic photons undergo only a few scattering events and, therefore, their direction is not fully randomized. The semiballistic contribution to the reflectance is thus more sensitive to the details of the phase function. To capture the influence of the phase function on the measured reflectance, we incorporate the previously derived phase function parameter p_{sb} [24] into our model.

2.1.1.   Diffuse reflectance $R_{SFR,dif}$

For the contribution of diffuse photons to the reflectance, we make use of the diffusion approximation to the radiative transport equation, which describes the reflectance versus radial distance, $R(\rho)$, for a pencil beam illumination. The implementation of the radiative transport equation for an overlapping source and detection fiber was derived by Faber et al., which models the diffuse reflectance as a single integral over the fiber diameter [26], where the integral of the diffuse reflectance versus radial distance is performed over the probability density function of distances over the fiber face $p(\rho)$:

$$R_{dif} = \frac{\pi}{4} \cdot d^2 \cdot \int_0^d R(\rho) \cdot p(\rho, d) \, d\rho \tag{3}$$

and

$$p(\rho, d) = \frac{16\rho}{\pi d^2} \cos^{-1}\left(\frac{\rho}{d}\right) - \frac{16}{\pi d}\left(\frac{\rho}{d}\right)^2 \sqrt{1 - \left(\frac{\rho}{d}\right)^2} \tag{4}$$

Equation (4) describes the distribution of distances between two randomly placed points on a disk with diameter d, which is a classic problem in the field of geometric probability [26,27]. For $R(\rho)$ we will use the diffuse reflectance versus radial distance as a function of the reduced scattering coefficient and the absorption coefficient for a pencil beam illumination using the extended boundary condition as proposed by Farrell et al. [28]:

$$R\left(\rho, \mu_s', \mu_a\right) = \frac{a'}{4\pi}\left[z_0\left(\mu_{eff} + \frac{1}{r_1}\right)\frac{e^{-\mu_{eff}\cdot r_1}}{r_1^2} + (z_0 + 2z_b)\left(\mu_{eff} + \frac{1}{r_2}\right)\frac{e^{-\mu_{eff}\cdot r_2}}{r_2^2}\right] \tag{5}$$

where a'= μ_s'/(μ_s'+μ_a); z_0=1/(μ_s'); μ_{eff} = √(3$\mu_a\mu_s$'); r_1 = √(z_0^2+ρ^2) and r_2 = √((z_0+2z_b)^2+ρ^2) ; z_b=2A/(3μ_s'); and A is a parameter that depends on the refractive index mismatch between the fiber and the tissue [29]. The diffuse contribution to the reflectance R_{dif} can be rewritten as a function of both μ_s'd and μ_a/μ_s' (the full derivation is provided in the Supplemental Materials). Since the diffuse contribution to the reflectance, R_{dif}, is a function of both μ_s'd and μ_a/μ_s', it does not depend on μ_s', μ_a and d separately, but on μ_s'd and μ_ad. This is demonstrated in Fig. 1, with calculations of R_{dif} using Eqs. (3)–(5) for different values of μ_s', μ_a and d, while holding μ_s'd and μ_ad constant.

Not all diffuse photons that reach the fiber face will be transported through the fiber to the detector. Only photons that arrive at an angle smaller than or equal to the acceptance angle of the fiber (θ_{acc}) will be detected, where θ_{acc} = asin(NA/n), NA is the fiber numerical aperture and n is the tissue refractive index. The fraction of photons arriving at the fiber face that is detected is described by the collection efficiency η_c [30]. Thus, the diffuse reflectance ($R_{SFR,dif}$) equals the collection efficiency of the fiber (η_c) times the fraction of diffuse photons that reach the fiber face (R_{dif}):

$$R_{SFR,dif} = \eta_c \cdot R_{dif} \tag{6}$$

We have previously shown that the collection efficiency for SFR spectroscopy equals η_c = (NA/n)^2·1.11 [24].

2.1.2.   Ratio semiballistic to diffuse photons X

In Eq. (1), X is the ratio between the semiballistic and diffuse reflectance. Since semiballistic photons undergo only a few scattering events before detection, the semiballistic reflectance is sensitive to the tissue phase function $p(\theta)$. Therefore, the influence of the phase function on the semiballistic reflectance needs to be captured in the formula for X. Previously, we introduced the
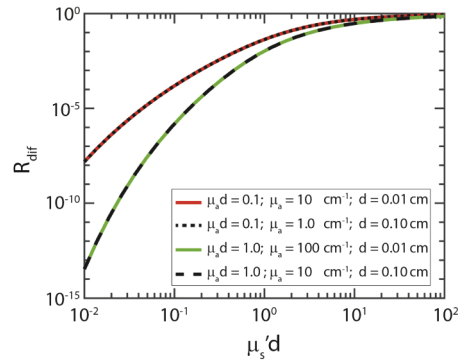
Fig. 1. Diffuse reflectance values (R_{dif}) calculated using Eqs. (3)–(5), for different values of μ_s', μ_a, and d. The diffuse reflectance is a function of μ_s'd and μ_a/μ_s'.

parameter p_{sb} to model the semiballistic contribution to the reflectance [24]:

$$p_{sb} = \frac{p_b(1°)}{1 - p_f(23°)} \tag{7}$$

where $p_b(1°)$ is the probability of a photon undergoing a scattering event between 0 and 1 degrees in the backward direction. This probability equals the integral over the phase function over 1 degree in the backward direction:

$$p_b(1°) = 2\pi \int_{-1°}^{0} p(\theta)sin\theta d\theta \tag{8}$$

$p_f(23°)$ is the probability of a photon undergoing a scattering event between 0 and 23 degrees in the forward direction:

$$p_f(23°) = 2\pi \int_{0}^{23°} p(\theta) sin\theta d\theta \tag{9}$$

In short, the parameter p_{sb} describes the detection probability of photons that undergo a single backscatter event and multiple forward scattering events (photons that we defined as semiballistic). The integration angles were based on an analysis of MC simulations employing a large range of phase functions. To ensure the simulated reflectance was in the semiballistic regime, we had used a low reduced scattering coefficient (μ_s'd = 0.1) and no absorption in the MC simulations. The full derivation of p_{sb} and the choice of integration angles can be found in [24].

To derive a model for the ratio X in the presence of absorption, we start from the observation that the reflectance can be written as the product of the reflectance in the absence of absorption (R_0) and the integral of the photon path length distribution (p(l)) weighted by the Beer-Lambert law:

$$R(\mu_a) = R_0 \cdot \int_{0}^{\infty} p(l) e^{-\mu_a l} dl \tag{10}$$

Equation (10) takes the form of a Laplace transform, with the absorption coefficient and path length as conjugate variables. In diffusion theory, the path length distribution p(l) depends on μ_s'l only. Using the scaling properties of the Laplace transform, this implies that the diffuse reflectance, $R_{dif}(\mu_a)$, will depend on the ratio μ_a/μ_s'. Since path lengths of semi-ballistic photons are much shorter than path lengths of diffuse photons, we assume that absorption will mainly influence the diffuse contribution to the reflectance. Therefore, we multiply the numerator of X in the absence of absorption (X_0, as derived in [24] for an NA of 0.22) by a function that includes the term μ_a/μ_s'.

$$X = X_0 \cdot f\left(\frac{\mu_a}{\mu_s'}\right) = 3046\left(\frac{p_{sb}}{(\mu_s'd)^2}\right)^{0.748} \cdot f\left(\frac{\mu_a}{\mu_s'}\right) \tag{11}$$

2.2. Monte Carlo simulations

We will develop a model for $f(\mu_a/\mu_s')$ based on MC simulations. Photons were launched at locations based on a uniform distribution across the fiber with an angle from a uniform angular distribution within the acceptance angle of the fiber θ_{acc}, where $\theta_{acc} = \arcsin(NA/n)$. Photons were detected if they reached the fiber face at an angle within θ_{acc}. For all MC simulations, the NA was 0.22 and the refractive index was 1.35 for the tissue, 1.45 for the fiber face, and 1.00 for the medium above the tissue. We ran each simulation three times and had chosen the number of launched photons such that the standard deviation over the mean of the reflectance for each set of three simulations was less than approximately 2%.

To derive the model for $f(\mu_a/\mu_s')$ in Eq. (11) of our model, we performed simulations with 10 different phase functions (Table 1), chosen such that they cover a wide range of p_{sb} values, g_1 values, and phase function types. With these phase functions, we performed simulations for a fiber diameter of 0.01 cm, with 20 values of μ_s' from 10 to 10000 cm^{-1} (equally spaced in 20 steps on a logarithmic scale) and 68 values of μ_a between 0.1 and 500 cm^{-1} (0.1 to 1 in steps of 0.1, 1 to 10 in steps of 1, 10 to 500 in steps of 10).

Table 1. 10 phase functions used to derive the model. Three types of phase functions were used: Reynolds McCormick (RMC), two-term Henyey Greenstein (TTHG), and modified Henyey Greenstein (MHG). Per phase function, p_{sb}, and g_1 values are given, as well as the parameters employed in the phase functions (α, g_R, g_f, g_b, and g_{HG}).

Phase function	p_{sb}	g_1	α	g_R	g_f	g_b	g_{HG}
RMC	$2.04 \cdot 10^{-6}$	0.83	2.2233	0.5053			
RMC	$2.94 \cdot 10^{-6}$	0.87	1.3933	0.6713			
RMC	$4.92 \cdot 10^{-6}$	0.71	2.2233	0.3953			
RMC	$8.02 \cdot 10^{-5}$	0.66	1.6700	0.4140			
RMC	$1.48 \cdot 10^{-5}$	0.82	0.2867	0.8927			
TTHG	$2.52 \cdot 10^{-5}$	0.52	0.9500		0.55	-0.15	
TTHG	$5.12 \cdot 10^{-5}$	0.85	0.9000		0.95	-0.05	
TTHG	$8.80 \cdot 10^{-5}$	0.84	0.9100		0.95	-0.25	
MHG	$1.19 \cdot 10^{-4}$	0.65	0.7722				0.8456
MHG	$2.10 \cdot 10^{-4}$	0.64	0.6633				0.8456

To determine the accuracy of our model for a wide range of phase functions, we performed additional simulations using the following 207 phase functions: 15 modified Henyey Greenstein (MHG), 146 two-term Henyey-Greenstein (TTHG), and 46 Reynolds McCormick phase functions (RMC), employing the parameters specified in Table 2 and applying the restrictions $g_1 \geq 0.5$ and $g_2 < 0.9$ to exclude biologically unreasonable phase functions. These restrictions resulted in phase functions with fairly equally distributed g_1 values between 0.5 and 0.94. We performed simulations for a fiber diameter of 0.01 cm and all the combinations of $\mu_a = [1,5,10,30, 100]$ cm^{-1}, $\mu_s' = [1,10, 50, 100]$ cm^{-1}, as well as for a fiber diameter of 0.1 cm and all the combinations of $\mu_a = [1,5,10,30]$ cm^{-1}, $\mu_s' = [1,10, 50, 100]$ cm^{-1}, resulting in 36 sets of simulations, with 207 phase functions each. We tested the accuracy of our model for the combination of the set of 10 phase functions and the set with 207 phase functions (21052 simulations in total). We compared this to the accuracy obtained with the currently used model of Kanick et al. [14,15].

To demonstrate the use of our model to determine optical properties from SFR spectra, we performed MC simulations with optical properties that can be encountered in tissue and performed a fit on these spectra using our model. We modeled spectra of two tissues, from 400 to 900 nm in steps of 5 nm. We based the reduced scattering coefficients and absorption coefficients on the review by Jacques [31], which are summarized in Table 4. The first tissue was

Table 2. Parameters employed in the selection of the 207 phase function used to determine the accuracy of our model.

| Phase function	Parameters
modified Henyey Greenstein	$0.01 \leq g_{HG} \leq 0.95$, 10 linear steps
	$0.01 \leq \alpha \leq 0.99$, 10 linear steps
two-term Henyey Greenstein	$0.5 \leq \alpha \leq 0.9$, 3 linear steps
	$0.91 \leq \alpha \leq 0.99$, 5 linear steps
	$0.05 \leq g_f \leq 0.95$, 10 linear steps
	$-0.95 \leq g_b \leq -0.05$, 5 linear steps
Reynolds McCormick	$0.01 \leq \alpha \leq 2.5$, 10 linear steps
	$0.01 \leq g_R \leq 0.95\text{-}0.2 \cdot \alpha$, 10 linear steps

simulated to resemble skin, with $\mu_s' = 46(\lambda/500)^{-1.421}$ cm^{-1}, a blood volume fraction of 0.01, an oxygen saturation level of 98%, and an MHG phase function where g_1 increases linearly over the wavelengths from 0.7 to 0.77. The second tissue that we simulated resembles soft tissue, with $\mu_s' = 18.9(\lambda/500)^{-1.3}$ cm^{-1}, a blood volume fraction of 0.05, an oxygen saturation level of 98%, and a TTHG with $\alpha = 0.95$, $g_b = -0.05$, and g_f linearly increasing over the wavelengths from 0.85 to 0.9.

For robust fit results, the number of fit parameters should be substantially smaller than the number of data points. Therefore, we performed MC simulations of spectra for two different fiber diameters. This implementation of SFR is referred to as multi-diameter SFR (MD-SFR) [3]. We performed simulations with fiber diameters of 300 and 600 microns. For a single SFR measurement, the number of data points (reflectance values) equals the number of wavelengths, i. Clearly, separate values for μ_s', μ_a, and p_{sb} per wavelength cannot be determined directly using a fit on a single SFR spectrum since the number of fit parameters would equal 3i. Therefore, we reduce the number of fit parameters by modeling the reduced scattering coefficient as $\mu_s' = a \cdot (\lambda/500)^{-b}$, where a is the scattering amplitude and b the scattering slope. The absorption coefficient is modeled as a sum of absorption spectra of different absorbers present in the tissue times the concentration of these absorbers: $\mu_{a,tissue} = \Sigma c_j \cdot \mu_{a,j}(\lambda)$, e.g. for tissue with blood and water: $\mu_{a,tissue} = c_{blood} \cdot \mu_{a,blood}(\lambda) + c_{water} \cdot \mu_{a,water}(\lambda)$. Since the wavelength-dependence of p_{sb} is unknown, we fit a value of p_{sb} for each wavelength within the spectrum. For a single measured spectrum, the number of data points equals i and the number of fit parameters equals 2+i + j (2 for μ_s', i for p_{sb}, and j for the number of absorbers, respectively). Such an under-determined system will not provide robust fit results. The use of two separate measurements with two fibers of different diameters overcomes this issue. In that case, the number of data points will equal 2i, while the number of fit parameters remains 2+i + j.
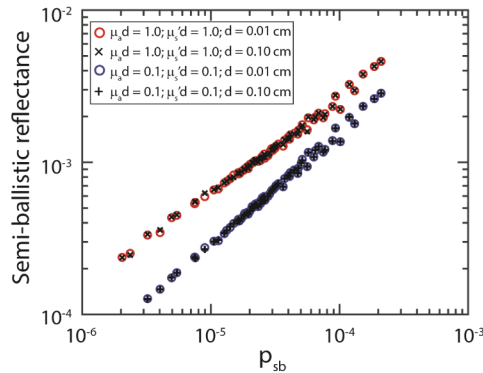
3. Results

Figure 2 shows the simulated reflectance as a function of $\mu_s'd$ for three different values of p_{sb} (colored lines) and two different values of μ_ad. The dashed black line indicates the diffuse reflectance ($R_{SFR,dif}$) for the corresponding $\mu_s'd$ and μ_ad values. For high values of $\mu_s'd$ the reflectance equals the diffuse reflectance (dashed line). For lower values of $\mu_s'd$ there is an additional semiballistic contribution to the reflectance. With increasing p_{sb} and μ_ad the fraction of semiballistic photons increases.

The diffuse contribution to the reflectance depends on $\mu_s'd$ and μ_ad only. To investigate whether the semiballistic contribution to the reflectance can be modeled as a function of $\mu_s'd$, μ_ad and p_{sb}, we compared the semiballistic reflectance for simulations with different values of μ_s' and μ_a, but the same values of $\mu_s'd$, μ_ad for all 207 phase functions (Table 2). Here, the semiballistic
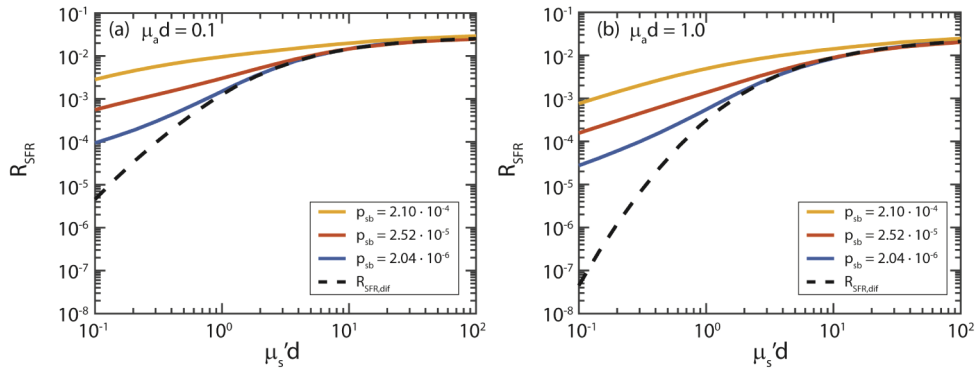
Fig. 2. Reflectance vs. μ_s'd for three different phase functions and (a) μ_ad = 0.1, (b) μ_ad = 1.0. For lower values of μ_s'd, an additional semiballistic reflectance is added to the diffuse reflectance ($R_{SFR,dif}$), which depends on p_{sb}, μ_s'd, and μ_ad.

reflectance is the simulated reflectance minus $R_{SFR,dif}$. Figure 3 shows the results for μ_s'd = 1.0 and μ_ad = 1.0, as well as for μ_s'd = 0.1 and μ_ad = 0.1 – using two different fiber diameters of 0.01 and 0.1 cm. The semiballistic reflectance values for the same μ_s'd, μ_ad, and phase functions nearly overlap. Therefore, we will model the semiballistic contribution to the reflectance using μ_s'd, μ_ad, and p_{sb}. The small differences in the reflectance can be explained by the fact that there is an uncertainty in our measured reflectance because we performed MC simulations such that the standard deviation over the mean of 3 simulations was less than 2%. It can be seen that for higher values of p_{sb}, there is some variation in the reflectance for the same p_{sb} values. This variation will likely result in a less accurate model for higher values of p_{sb}.

Fig. 3. The semiballistic reflectance depends on μ_s'd μ_ad and p_{sb}. Here, the semiballistic reflectance equals the simulated reflectance minus $R_{SFR,dif}$. For visualization purposes, simulation results for every 3rd p_{sb} value are depicted here.

Based on our simulations we searched for a model for $f(\mu_a/\mu_s')$ based on visual inspection of the data. Figure 4 shows an example of the visualization of two sets of simulations, with μ_s'd = 0.1 and 0.144, with μ_ad values of 0.001 to 1 and an MHG phase function. Based on the visual inspection we arrived at the following model:

$$f\left(\frac{\mu_a}{\mu_s'}\right) = e^{b_1 \cdot \left(\frac{\mu_a}{\mu_s'}\right)^{b_2}} \tag{12}$$
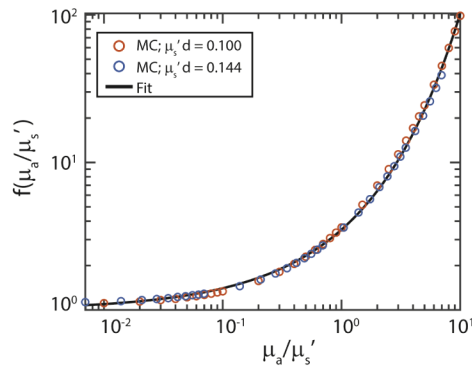
Fig. 4. We searched for a model for $f(\mu_a/\mu_s')$ based on visual inspection of the simulation results, where $f(\mu_a/\mu_s') = X/X_0$ (Eq. (11)). Here we show an example for simulations with the MHG phase function with $g_{HG} = 0.8456$ and $\alpha = 0.64$, $\mu_a d = 0.001$-1 and two values of $\mu_s'd = 0.100$ and 0.144. Black line: fit of Eq. (12). For this specific set of simulations $b_1 = 1.25$ and $b_2 = 0.57$. For the full model, we determined $b_{1,2}$ based on all MC simulations.

We determined optimal values of $b_{1,2}$ (Table 3) based on fitting our entire model (Eqs. (1)–(9) and (11)) to the MC simulations for the set of 10 phase functions (Table 1).

Figure 5 shows the simulated reflectance versus the modeled reflectance for the combination of the set of 10 phase functions and the set with 207 phase functions (using $b_{1,2}$ from Table 3). For our model [Fig. 5(a)] the median error is 5.6% with a standard deviation of 8.8%. Figure 5(b) shows the results for the model of Kanick et al., where the median error is 19.3%, with a standard deviation of 43.2%.
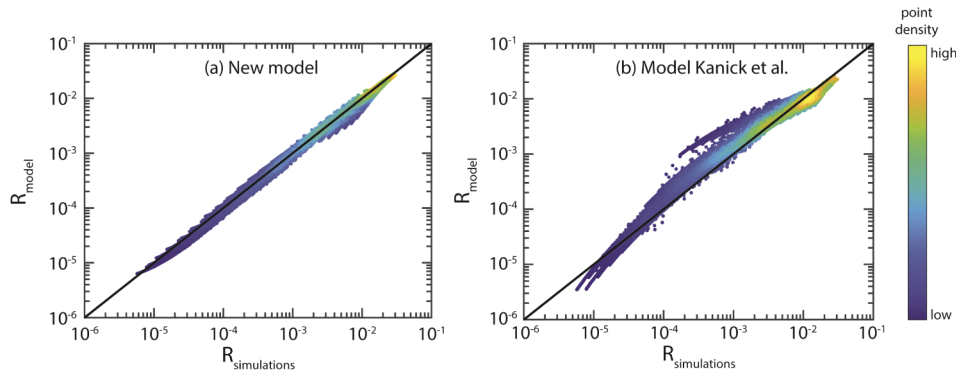
Fig. 5. Reflectance as predicted by the model (R_{model}) versus the reflectance obtained from the MC simulations ($R_{simulations}$). The black line depicts a perfect prediction. Since many points overlap, colors are used to indicate the density of points (blue = low, yellow = high). (a) For our model, the median error is 5.6% with a standard deviation of 8.8%. (b) For the model of Kanick et al. the median error is 19.3% with a standard deviation of 43.2%.

To obtain a better understanding of the relationship between the error in the reflectance and the optical properties, Fig. 6 depicts color maps of the median error in the reflectance versus $\mu_s'd$, $\mu_a d$, and p_{sb} for the simulations with 10 phase functions. For a large range of optical properties, the median error is below 10%. Median errors increase up to 25% for $\mu_a d$ values above 4, in combination with lower values of $\mu_s'd$ below 5. Also, median errors increase above 20% for high values of p_{sb} in combination with $\mu_s'd$ values above 3. We determined the median error for each

Table 3. Resulting parameters $b_{1,2}$ based on fitting our entire model (Eqs. (1)–(9) and (11)) to the MC simulations for the set of 10 phase functions (Table 1). The 95% confidence intervals on these fit parameters are indicated.

	Value	95% CI
b_1	1.17	(±0.004)
b_2	0.57	(±0.001)

type of phase function for the 36 sets of simulations with the 207 phase functions (Table 2). The median errors were 6.4% for the TTHG, 8.6% for the MHG, and 5.1% for the RMC.
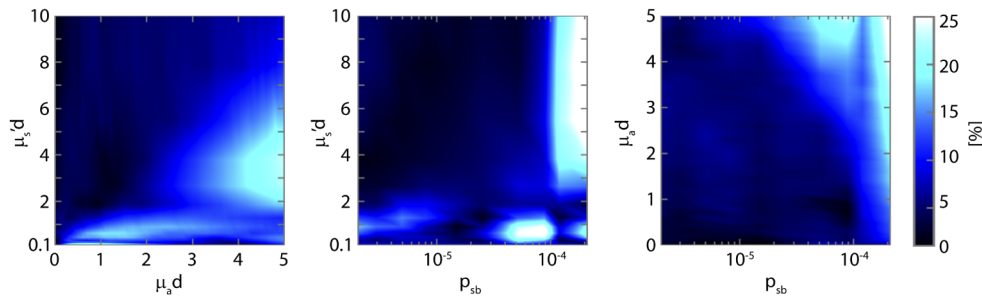

Fig. 6. Color maps of the relative median error in the reflectance versus $\mu_s'd$, $\mu_a d$ and p_{sb}, for the set of simulations with 10 phase functions. To provide a clearer image, the median error values have been interpolated to a finer grid of $\mu_s'd$, $\mu_a d$, and p_{sb} values. Note the vertical axis for $\mu_s'd$ starting at a value of 0.1, since that was the minimum value of $\mu_s'd$ used in the simulations.

Figure 7 shows two sets of simulated tissue spectra and the fit results for μ_s', μ_a, and p_{sb}. Table 4 lists the resulting fit parameters related to blood (blood volume fraction and oxygen saturation) and scattering (scattering amplitude and slope). For both simulated tissues the fit results for μ_s' are very close to the simulated μ_s' values [Figs. 7(c), 7(h)]. The average differences in μ_s' over all wavelengths were 7% and 4% for tissue 1 and 2, respectively. The difference in the blood volume fraction was 20% for tissue 1 and 2% for tissue 2. The blood oxygenation was underestimated by 1% for tissue 1 and overestimated by 2% for tissue 2. The average differences in p_{sb} over all wavelengths were 9% and 4% for tissue 1 and 2, respectively [Figs. 7(e), 7(j)]. Comparing the fit result for μ_a [Figs. 7(d), 7(i)] and p_{sb}, it seems that these fit parameters are competing. The absorption dips of hemoglobin are visible in the fit results for p_{sb}.

Table 4. Input parameters and fit parameter results for simulated spectra for skin (Fig. 7(a-e)) and soft tissue (Fig. 7(f-j))

	Skin		Soft tissue	
	Simulation	Fit	Simulation	Fit
Oxygen saturation	98.0%	96.6%	98.0%	99.8%
Blood volume fraction	0.010	0.008	0.050	0.051
Scattering amplitude [cm^{-1}]	46.0	42.6	18.9	19.0
Scatter slope	1.421	1.424	1.300	1.441
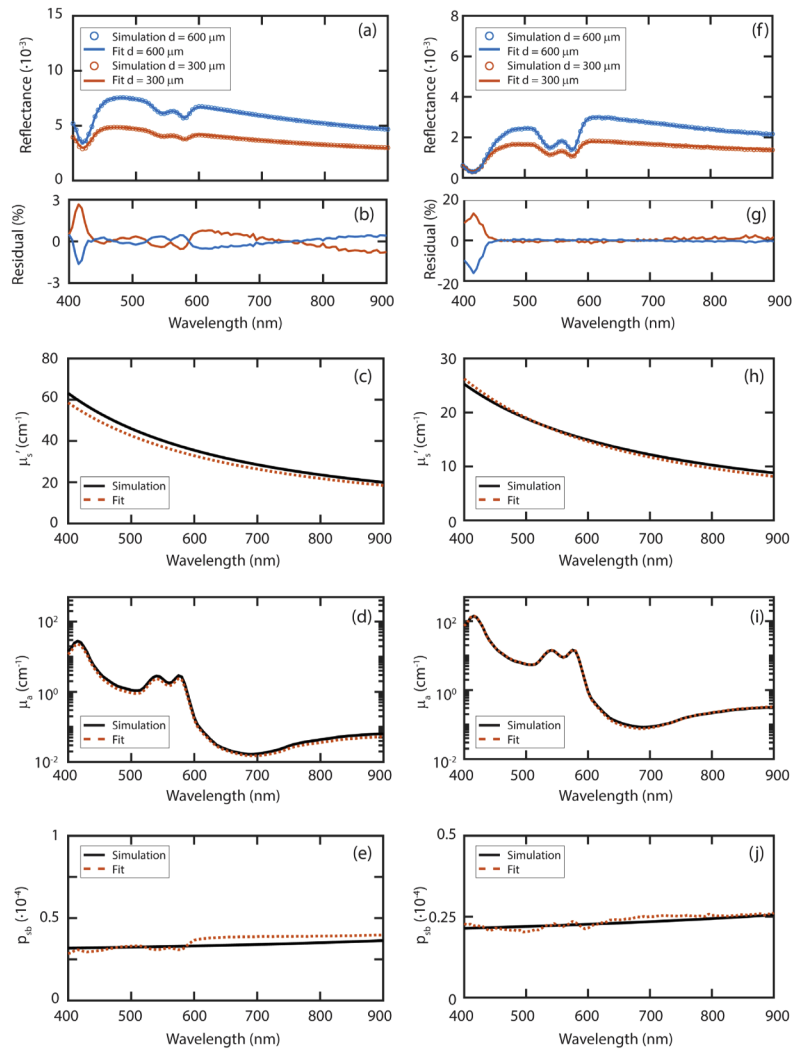
Fig. 7. Fit on simulated spectra for skin (a) and soft tissue (f) and their fit residuals (b) and (g), respectively. Fit results for μ_s' (c,h), μ_a (d,i) and p_{sb} (e,j) are shown here. Black lines indicate the simulated values, dashed red lines indicate the fit results. Input and fit parameters are in Table 4.

4. Discussion

SFR spectroscopy is a spectroscopic technique especially suitable to detect small-scale changes in tissue. From the measured reflectance, tissue optical properties can be extracted and related to the disease state of tissue. However, the currently used model of Kanick et al. [14] to obtain optical properties from SFR measurements is limited to tissues with MHG phase functions. However, many tissues have different types of phase functions and often the phase function of a specific tissue under investigation is not known. Therefore, a model that is valid for a wide range of tissue phase functions is vital. Here, we developed a comprehensive model for the SFR reflectance as a function of both scattering and absorption properties of tissue that provides accurate results for a wide range of tissue phase functions. This new model predicts the measured reflectance substantially better compared to the model of Kanick et al. [14] (5.6 vs. 19.3% median error) and is valid for a wider range of phase functions.

We modeled the diffuse contribution to the reflectance by solving the model for spatially resolved reflectance of Farrell et al. [28] for an overlapping source and detection fiber [26] by integrating over the probability density function of distances over the fiber face. For the diffuse reflectance in the absence of absorption, a closed form of R_{dif} has been derived [26], but this has not yet been done in the presence of absorption. If a closed form of R_{dif} is derived this could increase the speed of a fitting procedure for MDSFR spectra. Here, we showed that the diffuse reflectance depends on $\mu_s'd$ and μ_a/μ_s', and using MC simulations, we determined that the total reflectance can be described using $\mu_s'd$, μ_ad, and p_{sb}.

We investigated the median error in the reflectance versus $\mu_s'd$, μ_ad, and p_{sb}. For a large range of optical properties, the median error was below 10%. Median errors increase above 20% from a μ_ad value of 4, in combination with lower values of $\mu_s'd$ below 5. The main absorbers in tissue are blood, fat, and water. A μ_ad value above 4 will not be reached as a result of the fat or water content of tissue. For pure fat the highest absorption coefficient from 400-1100 nm is 0.13 cm^{-1} [32], for a large fiber diameter of 0.1 cm, this would result in a μ_ad value of 0.013. For pure water, assuming a large fiber diameter of 0.1 cm, μ_ad only becomes larger than 4 for wavelengths above 1880 nm [33]. The increased errors for $\mu_ad > 4$ are relevant for the absorption by blood. The absorption spectrum of blood has one high peak from 400-450 nm and two lower peaks from 500-600 nm. To increase the range of blood volume fractions for which the model accurately predicts the absorption, a smaller fiber can be used. For a fiber diameter of 0.05 cm, a blood volume fraction of 28% will still result in $\mu_ad < 4$ for the spectrum above 450 nm [34]. For most tissue types, the blood volume fraction is in the order of 1-5% [31], therefore, the model will provide accurate results for the spectrum above 450. The blood absorption spectrum also has a high peak from 400-450 nm. Assuming a fiber diameter of 0.05 cm, μ_ad will be below 4 from 400-450 nm for blood volume fractions up to 3%. Nevertheless, the entire absorption spectrum of blood is fitted to a measured SFR spectrum. Therefore, we expect that even for higher blood volume fractions the fit will provide accurate estimates of the blood volume fraction since the majority of the spectrum will be accurately modeled. This is demonstrated by our results for the simulated tissue with a blood volume fraction of 5%. Even though the residual of the fit was high for 400-450 nm (Fig. 7(g)), the fit result for the blood volume fraction was accurate (Table 4).

We also found that median errors increase above 20% for high values of p_{sb} in combination with $\mu_s'd$ value s above 3. These higher errors can be explained by the fact that for higher values of p_{sb} there is more variation in the reflectance values obtained for different phase functions with similar p_{sb} values (Fig. 3). Higher errors for higher values of p_{sb} are thus an inevitable result when p_{sb} is used to model SFR measurements. Nevertheless, we showed previously that the variation in the reflectance was lowest for p_{sb}, compared to other parameters (σ [35], γ [36], δ [37] and R_{pNA} [25]) that have been used to incorporate the phase function influence into models for subdiffuse reflectance [24]. Therefore, modeling the reflectance using p_{sb} will provide more accurate results than using σ, γ, δ and R_{pNA}.

To extract optical properties from SFR measurements, we used two different fiber diameters in an approach known as MDSFR. In our analysis in this paper, we assumed that both fibers sample a volume with the same optical properties. In clinical applications, when the two fibers are placed next to each other and tissue is inhomogeneous, this is not necessarily the case. Compared to DRS – where it is also assumed the tissue within the sampling volume is homogenous – MDSFR has the advantage that the sampling volume is much smaller and, therefore, the assumption of a homogenous sampling volume is more likely to hold. If two fibers are placed next to each other, the sampling volume will be shifted sideways with respect to the tissue surface by only a few hundred micrometers. Nevertheless, in MDSFR measurements the larger fiber will sample a deeper tissue volume, which is especially relevant for the absorption of light by the microvasculature. This can be accounted for by fitting separate parameters related to absorption for each fiber diameter [38].

For the MDSFR approach in this paper, we modeled the reduced scattering coefficient as $\mu_s' = a \cdot (\lambda/500)^{-b}$ and the absorption coefficient as a sum of absorption spectra of different absorbers present in the tissue times the concentration of these absorbers. Currently, the wavelength dependence of the phase function in general, and p_{sb} specifically, is not well-characterized. Therefore, a value of p_{sb} was fitted for each wavelength in the spectrum. It seems that μ_a and p_{sb} currently compete in the fit, leading to less accurate results. The robustness of the fit is expected to increase if a model for p_{sb} is used that decreases the number of fit parameters.

5. Conclusion

We developed a model for SFR spectroscopy to describe the reflectance as a function of tissue scattering and absorption properties, which provides accurate results over a wide range of phase functions. The new model predicts the measured reflectance substantially better compared to the currently used model of Kanick et al. [14] which was developed for tissues with MHG phase functions only. The phase function of a specific tissue under investigation is generally not known. Therefore, a model that is valid for the wide range of phase functions that can be encountered in tissue is essential.

Funding

Disclosures

The authors declare no conflicts of interest.

See Supplement 1 for supporting content.

References

1. D. Piao, K. L. McKeirnan, N. Sultana, M. A. Breshears, A. Zhang, and K. E. Bartels, "Percutaneous single-fiber reflectance spectroscopy of canine intervertebral disc: Is there a potential for in situ probing of mineral degeneration?" Lasers Surg. Med. **46**(6), 508–519 (2014).
2. P. L. Stegehuis, L. S. F. Boogerd, A. Inderson, R. A. Veenendaal, P. van Gerven, B. A. Bonsing, J. Sven Mieog, A. Amelink, M. Veselic, H. Morreau, C. J. H. van de Velde, B. P. F. Lelieveldt, J. Dijkstra, D. J. Robinson, and A. L. Vahrmeijer, "Toward optical guidance during endoscopic ultrasound-guided fine needle aspirations of pancreatic masses using single fiber reflectance spectroscopy: a feasibility study," J. Biomed. Opt. **22**(2), 024001 (2017).
3. U. A. Gamm, M. Heijblom, D. Piras, F. M. Van den Engh, S. Manohar, W. Steenbergen, H. J. C. M. Sterenborg, D. J. Robinson, and A. Amelink, "In vivo determination of scattering properties of healthy and malignant breast tissue by use of multi-diameter-single fiber reflectance spectroscopy (MDSFR)," Proc. SPIE **8592**, 85920T (2013).

4. O. Bugter, J. A. Hardillo, R. J. Baatenburg de Jong, A. Amelink, and D. J. Robinson, "Optical pre-screening for laryngeal cancer using reflectance spectroscopy of the buccal mucosa," Biomed. Opt. Express **9**(10), 4665 (2018).

5. O. Bugter, M. C. W. Spaander, M. J. Bruno, R. J. Baatenburg De Jong, A. Amelink, and D. J. Robinson, "Optical detection of field cancerization in the buccal mucosa of patients with esophageal cancer," Clin. Transl. Gastroenterol. **9**(4), e152 (2018).

6. F. van Leeuwen-van Zaane, U. A. Gamm, P. B. A. A. van Driel, T. J. A. Snoeks, H. S. de Bruijn, A. van der Ploeg-van den Heuvel, I. M. Mol, C. W. G. M. Löwik, H. J. C. M. Sterenborg, A. Amelink, and D. J. Robinson, "In vivo quantification of the scattering properties of tissue using multi-diameter single fiber reflectance spectroscopy," Biomed. Opt. Express **4**(5), 696 (2013).

7. T. Sun, C. A. Davis, R. E. Hurst, J. W. Slaton, and D. Piao, "Orthotopic AY-27 rat bladder urothelial cell carcinoma model presented an elevated methemoglobin proportion in the increased total hemoglobin content when evaluated in vivo by single-fiber reflectance spectroscopy," Proc. SPIE **10038**, 100380L (2017).

8. S. Hariri Tabrizi, S. Mahmoud Reza Aghamiri, F. Farzaneh, A. Amelink, and H. J. C. M. Sterenborg, "Single fiber reflectance spectroscopy on cervical premalignancies: the potential for reduction of the number of unnecessary biopsies," J. Biomed. Opt. **18**(1), 017002 (2013).

9. L. Yu, Y. Wu, J. F. Dunn, and K. Murari, "In-vivo monitoring of tissue oxygen saturation in deep brain structures using a single fiber optical system," Biomed. Opt. Express **7**(11), 4685 (2016).

10. D. Piao, K. McKeirnan, Y. Jiang, M. A. Breshears, and K. E. Bartels, "A low-cost needle-based single-fiber reflectance spectroscopy method to probe scattering changes associated with mineralization in intervertebral discs in chondrodystrophoid canine species - A pilot study," Photonics Lasers Med. **1**(2), 103–115 (2012).

11. J. R. Mourant, J. Boyer, A. H. Hielscher, and I. J. Bigio, "Influence of the scattering phase function on light transport measurements in turbid media performed with small source-detector separations," Opt. Lett. **21**(7), 546–548 (1996).

12. T. Sun and D. Piao, "Simple analytical total diffuse reflectance over a reduced-scattering-pathlength scaled dimension of $[10^{-5}, 10^{-1}]$ from a medium with HG scattering anisotropy," Appl. Opt. **58**(33), 9279 (2019).

13. S. C. Kanick, U. A. Gamm, M. Schouten, H. J. C. M. Sterenborg, D. J. Robinson, and A. Amelink, "Measurement of the reduced scattering coefficient of turbid media using single fiber reflectance spectroscopy: fiber diameter and phase function dependence," Biomed. Opt. Express **2**(6), 1687–1702 (2011).

14. S. C. Kanick, U. A. Gamm, H. J. C. M. Sterenborg, D. J. Robinson, and A. Amelink, "Method to quantitatively estimate wavelength-dependent scattering properties from multidiameter single fiber reflectance spectra measured in a turbid medium," Opt. Lett. **36**(15), 2997–2999 (2011).

15. S. C. Kanick, D. J. Robinson, H. J. C. M. Sterenborg, and A. Amelink, "Monte Carlo analysis of single fiber reflectance spectroscopy: photon path length and sampling depth," Phys. Med. Biol. **54**(22), 6991–7008 (2009).

16. S. L. Jacques, C. A. Alter, and S. A. Prahl, "Angular dependence of HeNe laser light scattering by human dermis," Lasers Life Sci. **1**(4), 309–333 (1987).

17. R. Marchesini, A. Bertoni, S. Andreola, E. Melloni, and A. E. Sichirollo, "Extinction and absorption coefficients and scattering phase functions of human tissues in vitro," Appl. Opt. **28**(12), 2318 (1989).

18. P. Saccomandi, V. Vogel, B. Bazrafshan, E. Schena, T. J. Vogl, S. Silvestri, and W. Mäntele, "Estimation of anisotropy coefficient of swine pancreas, liver and muscle at 1064 nm based on goniometric technique," J. Biophotonics **8**(5), 422–428 (2015).

19. P. van der Zee, M. Essenpreis, D. T. Delpy, P. Van Der Zee, and M. Essenpreis, "Optical properties of brain tissue," in *Photon Migration and Imaging in Random Media and Tissues*, B. Chance and R. R. Alfano, eds. (1993), Vol. 1888, pp. 454–465.

20. N. Ghosh, S. K. Mohanty, S. K. Majumder, and P. K. Gupta, "Measurement of optical transport properties of normal and malignant human breast tissue," Appl. Opt. **40**(1), 176–184 (2001).

21. J. Zijp and J. ten Bosch, "Optical properties of bovine muscle tissue in vitro; a comparison of methods," Phys. Med. Biol. **43**(10), 3065–3081 (1998).

22. L. O. Reynolds and N. J. McCormick, "Approximate two-parameter phase function for light scattering," J. Opt. Soc. Am. **70**(10), 1206–1212 (1980).

23. A. N. Yaroslavsky, I. V. Yaroslavsky, T. Goldbach, and H. J. Schwarzmaier, "Optical properties of blood in the near-infrared spectral range," Proc. SPIE **2678**, 314–324 (1996).

24. A. L. Post, H. J. C. M. Sterenborg, F. G. Woltjer, T. G. van Leeuwen, and D. J. Faber, "Subdiffuse scattering model for single fiber reflectance spectroscopy," J. Biomed. Opt. **25**(01), 1 (2020).

25. A. L. Post, S. L. Jacques, H. J. C. M. Sterenborg, D. J. Faber, and T. G. van Leeuwen, "Modeling subdiffusive light scattering by incorporating the tissue phase function and detector numerical aperture," J. Biomed. Opt. **22**(5), 050501 (2017).

26. D. J. Faber, A. L. Post, H. J. C. M. Sterenborg, and T. G. Van Leeuwen, "Analytical model for diffuse reflectance in Single Fiber Reflectance Spectroscopy," Opt. Lett. **45**(7), 2078–2081 (2020).

27. H. Solomon, *Geometric Probability* (Society for Industrial and Applied Mathematics, 1978).

28. T. J. Farrell, M. S. Patterson, and B. Wilson, "A diffusion theory model of spatially resolved, steady-state diffuse reflectance for the noninvasive determination of tissue optical properties in vivo," Med. Phys. **19**(4), 879–888 (1992).

29. F. Martelli, S. Del Bianco, A. Ismaelli, and G. Zaccanti, *Light Propagation through Biological Tissue and Other Diffusive Media: Theory, Solutions, and Software* (SPIE, 2009).

30. P. R. Bargo, S. A. Prahl, and S. L. Jacques, "Collection efficiency of a single optical fiber in turbid media," Appl. Opt. **42**(16), 3187–3197 (2003).
31. S. L. Jacques, "Optical properties of biological tissues: a review," Phys. Med. Biol. **58**(14), 5007–5008 (2013).
32. R. L. P. van Veen, H. J. C. M. Sterenborg, A. Pifferi, A. Torricelli, and R. Cubeddu, "Determination of VIS- NIR absorption coefficients of mammalian fat, with time- and spatially resolved diffuse reflectance and transmission spectroscopy," in *Biomedical Topical Meeting* (OSA, 2004), p. SF4.
33. G. M. Hale and M. R. Querry, "Optical Constants of Water in the 200-nm to 200-μm Wavelength Region," Appl. Opt. **12**(3), 555 (1973).
34. S. Prahl, "Optical Absorption of Hemoglobin," https://omlc.org/spectra/hemoglobin/.
35. N. Bodenschatz, P. Krauter, A. Liemert, and A. Kienle, "Quantifying phase function influence in subdiffusively backscattered light," J. Biomed. Opt. **21**(3), 035002 (2016).
36. F. Bevilacqua and C. Depeursinge, "Monte Carlo study of diffuse reflectance at source–detector separations close to one transport mean free path," J. Opt. Soc. Am. A **16**(12), 2935 (1999).
37. P. Naglič, F. Pernuš, B. Likar, and M. Bürmen, "Estimation of optical properties from subdiffusive reflectance beyond the second similarity parameter γ," in *Diffuse Optical Spectroscopy and Imaging VI*, H. Dehghani and H. Wabnitz, eds. (2017), p. 1041205.
38. X. U. Zhang, P. van der Zee, I. Atzeni, D. J. Faber, T. G. van Leeuwen, and H. J. C. M. Sterenborg, "Multidiameter single-fiber reflectance spectroscopy of heavily pigmented skin: modeling the inhomogeneous distribution of melanin," J. Biomed. Opt. **24**(12), 127001 (2019).